IEEE Access
Multidisciplinary | Rapid Review | Open Access Journal

Received July 24, 2020, accepted August 4, 2020, date of publication August 17, 2020, date of current version August 27, 2020.

Digital Object Identifier 10.1109/ACCESS.2020.3017005

3-D Analytical Model of Armature Reaction Field of IPMSM With Multi-Segmented Skewed Poles and Multi-Layered Flat Wire Winding Considering Current Harmonics

CONGGAN MA[1,2], (Member, IEEE), JIAMING LI[1], HUICHAO ZHAO[3], (Member, IEEE), JINHAO WANG[3], XIANGRUI YIN[3], SHUGUANG ZUO[4], XUDONG WU[4], AND HAIFENG LU[1]

[1]School of Automotive Engineering, Harbin Institute of Technology at Weihai Campus, Weihai 264209, China
[2]State Key Laboratory of Robotics and System, Harbin Institute of Technology, Harbin 150001, China
[3]State Key Laboratory of Comprehensive Technology on Automobile Vibration and Noise and Safety Control, China First Automobile Works (FAW) Group, Changchun 130013, China
[4]School of Automotive Studies, Tongji University, Shanghai 201804, China

Corresponding author: Huichao Zhao (zhaohuichao@faw.com.cn)

This work was supported in part by the National Natural Science Foundation of China under Grant 51975141 and Grant 51605112, in part by the Natural Science Foundation of Shandong Province under Grant ZR2015EQ020, and in part by the 2018 Open Fund of State Key Laboratory of Comprehensive Technology on Automobile Vibration and Noise and Safety Control under Grant 2018-03.

ABSTRACT A 3-D analytical model of armature reaction field (ARF) of interior permanent magnet synchronous motor (IPMSM) with multi-segmented skewed poles (MSP) and multi-layered flat wire winding (MFWW) considering current harmonics is proposed in this paper. Firstly, based on the MFWW distribution analysis and the coil magnetic field vector superposition method, the ideal ARF functions of the MFWW considering low-order current harmonics and high-order sideband current harmonics are derived. Secondly, 3-D relative permeance functions caused by the stator slotting effect and the multi-segmented rotor magnetic barriers are presented. Thirdly, 3-D analytical expressions of ARF are obtained by multiplying the ideal ARF functions and the 3-D relative permeance functions. Additionally, the effects of low-order current harmonics, high order sideband current harmonics, MSP, and stator slotting on the spatial orders and frequencies of ARF are analyzed. Finally, the proposed model is verified by finite element method (FEM) and experiment.

INDEX TERMS Analytical model, armature reaction field, current harmonic, interior permanent magnet synchronous motor.

I. INTRODUCTION

Currently, interior permanent magnet synchronous motor (IPMSM) has been widely equipped in electric vehicles, due to its several advantages compared with surface permanent magnet synchronous motor (SPMSM), such as high flux-weakening capability, high torque output owing to the reluctance torque, and robust structure because of permanent magnets embedded in the rotor [1]. The multi-segmented skewed poles (MSP) and the multi-layered flat wire winding (MFWW) further enhance the performance of IPMSM. Firstly, step skewing of the rotor effectively reduces its cogging torque and torque ripple [2], [3]. Secondly, the MFWW, namely hairpin winding, achieves a higher fill factor, shorter end windings, higher power and torque density and lower copper loss [4], [5]. Furthermore, because of a better contact between conductors and between winding and iron core, a better cooling performance compared with traditional round wire winding is gained [6]. Therefore, IPMSM with MSP and MFWW has a promising prospect. However, current harmonics caused by nonsinusoidal back electromotive force (BEMF) and pulse width modulation (PWM) significantly influence the armature reaction field (ARF) of IPMSM, and further affect inductance, iron loss, torque, vibration and noise [7]–[9]. Consequently, an accurate prediction of ARF of IPMSM with MSP and

The associate editor coordinating the review of this manuscript and approving it for publication was Kan Liu.

MFWW considering current harmonics is vital to achieve a better performance [10].

Nowadays, finite element method (FEM) and analytical method are two main approaches to calculate ARF of IPMSM. The major advantage of FEM is its ability to consider a complex rotor structure [11] and magnetic saturation. However, it is time consuming [12]–[15], especially for 3-D models, which are required for IPMSM with MSP. Compared with FEM, analytical method can explicitly reveal the sources of spatial and temporal harmonics [10], [15], and effectively guides IPMSM design. There are three analytical methods to predict ARF of IPMSM, i.e., magnetic-equivalent-circuit method, subdomain method and magnetic-potential-and-permeance method:

1) In magnetic-equivalent-circuit method, magnetic resistances and magnetomotive forces of different areas need to be calculated at first. Then the magnetic circuit is compared to an electric circuit and finally the air-gap magnetic field density is obtained [14], [16], [17]. The effects of the complex rotor structures and the magnetic saturation on the ARF of IPMSM can be considered by magnetic-equivalent-circuit method. However, its accuracy is sensitive to the density of magnetic circuit nodes, and it can only predict the radial component of air-gap flux density but not the tangential component [18].

2) For subdomain method, IPMSM is usually divided into several areas, such as permanent magnets, slots, air-gap, and stator/rotor iron core. Then the governing partial differential equations based on Maxwell's equations are presented and solved. Finally, based on boundary conditions of different areas, coefficients of the general solution are determined and magnetic field distribution is obtained [9]–[11]. However, if permanent magnets are complexly embedded into the rotor, more subdomains are required for approximation. It complicates boundary conditions and makes equation solutions extremely complicated.

3) For magnetic-potential-and-permeance method, the ideal ARF without slotting is initially calculated by using winding coefficients [8], [15], [19] or the vector-addition method [20], [21]. Then the ARF with slotting can be calculated by multiplying the ideal ARF without slotting and the relative permeance function. Compared with magnetic-equivalent-circuit method and subdomain method, magnetic-potential-and-permeance method has simpler calculation processes, whereas its accuracy greatly relies on its relative permeance functions. There are several approaches to calculate the relative permeance functions. In [22], a subdomain method is adopted to calculate the relative permeance function of stator slots. In [23], a 2-D relative permeance can only predict the radial component of flux density but not the tangential component. In [12] and [21], the complex relative permeance based on conformal mapping can predict both kinds of flux density. However, the magnet barrier structure of step skewing rotors leads to the axial distribution variation of ARF, which is not considered in the references above. Moreover, few references take into account the effects of current harmonics on the ARF of IPMSM with MSP and MFWW.

In summary, a 3-D analytical model of ARF of IPMSM with MSP and MFWW considering current harmonics is required in order to meet the requirement of fast and accurate prediction. The remainder of this study is organized as follows. In Section II, based on the MFWW distribution analysis and the coil magnetic field vector superposition method, the ideal ARF functions of the MFWW considering low-order current harmonics and high-order sideband current harmonics are derived. Then, 3-D relative permeance functions caused by the stator slotting effect and the multi-segmented rotor magnetic barriers are presented. Finally, 3-D analytical expressions of ARF are obtained by multiplying the ideal ARF functions and the 3-D relative permeance functions. Additionally, the effects of low-order current harmonics, high order sideband current harmonics, MSP, and stator slotting on the spatial orders and frequencies of ARF are analyzed. In Section III, the proposed analytical model is directly verified by FEM and indirectly verified by measuring electromagnetic torque of an IPMSM.

II. ANALYTICAL MODELING

In order to illustrate the 3-D analytical modeling method of ARF, an IPMSM with 8 poles, 48 slots, 6 segmented skewed poles, and 4 layered flat wire windings is taken as a case. Its parameters are listed in Table 1.

TABLE 1. Parameters of IPMSM.

Parameters	Symbol	Value\Unit
Segment number	N_0	6
Flat wire layer number	C_0	4
Pole number	$2p$	8
Slot number	Q_s	48
Flat wire specifications	$a\times b$	3.2mm×2.6mm
PM remanence	B_r	1.282T
Outer stator radius	R_{so}	110mm
Inner stator radius	R_{si}	79.8mm
Stack length	L	130mm
Outer rotor radius	R_{ro}	79.1mm
Inner rotor radius	R_{ri}	22.5mm
Air gap length	g	0.7mm

A. LOW-ORDER CURRENT HARMONICS AND HIGH-ORDER SIDEBAND CURRENT HARMONICS

Generally, current harmonics can be divided into two categories: low-order current harmonics and high-order current harmonics [7]. The former are mainly derived from non-sinusoidal BEMF, which comes from non-sinusoidal

open-circuit air gap field (OCAGF), while the latter are mainly caused by PWM [7], [24], [25]. Besides the fundamental current, there are plenty of low-order current harmonics and high-order sideband current harmonics in the phase currents of IPMSM. Therefore, three phase currents can be expressed:

$$\begin{aligned} I_A(t) &= I_1 \sin(2\pi f_c t + \psi_1) + \sum_{h\neq 1} I_h \sin(2\pi h f_c t + \psi_h) \\ &+ \sum_n \sum_k \{I_{n,k,1} \sin[2\pi (a_n f_s + b_{n,k} f_c) + \psi_{n,k,1}] \\ &+ I_{n,k,2} \sin[2\pi (a_n f_s - b_{n,k} f_c) + \psi_{n,k,2}]\} \end{aligned} \tag{1}$$

$$\begin{aligned} I_B(t) &= I_1 \sin\left(2\pi f_c t + \psi_1 - \frac{2}{3}\pi\right) \\ &+ \sum_{h\neq 1} I_h \sin\left(2\pi h f_c t + \psi_h - \frac{2}{3}\pi\right) \\ &+ \sum_n \sum_k \{I_{n,k,1} \sin[2\pi (a_n f_s + b_{n,k} f_c) \\ &+ \psi_{n,k,1} - \frac{2}{3}\pi] + I_{n,k,2} \sin[2\pi (a_n f_s - b_{n,k} f_c) \\ &+ \psi_{n,k,2} - \frac{2}{3}\pi]\} \end{aligned} \tag{2}$$

$$\begin{aligned} I_C(t) &= I_1 \sin\left(2\pi f_c t + \psi_1 + \frac{2}{3}\pi\right) \\ &+ \sum_{h\neq 1} I_h \sin\left(2\pi h f_c t + \psi_h + \frac{2}{3}\pi\right) \\ &+ \sum_n \sum_k \{I_{n,k,1} \sin[2\pi (a_n f_s + b_{n,k} f_c) \\ &+ \psi_{n,k,1} + \frac{2}{3}\pi] + I_{n,k,2} \sin[2\pi (a_n f_s - b_{n,k} f_c) \\ &+ \psi_{n,k,2} + \frac{2}{3}\pi]\} \end{aligned} \tag{3}$$

where, I_1, f_c, and ψ_1 are amplitude, frequency, phase angle of the fundamental current, respectively, I_h and ψ_h are amplitude and phase angle of the h-order current harmonic, respectively, $I_{n,k,1}$ and $I_{n,k,2}$ are amplitudes of the high-order sideband current harmonics, $\psi_{n,k,1}$ and $\psi_{n,k,2}$ are phase angles of the high-order sideband current harmonics, a_n and $b_{n,k}$ are coefficients of the high-order sideband current harmonics, f_s is the switching frequency of PWM.

According to (1)-(3), the main frequencies of the low-order current harmonics and the high-order sideband current harmonics are hf_c and $a_n f_s \pm b_{n,k} f_c$ respectively.

B. IDEAL ARF OF MFWW

The cylindrical coordinate system O-$r\alpha z$ is established by taking the circle center of the end face of the stator core as the origin O, and $\alpha = 0$ pointing to the center of the slot opening of Slot 1, shown in Fig. 1.

In order to consider low-order current harmonics and high-order current harmonics, the radial and tangential ARF by the l^{th} coil can be expressed as Fourier series:

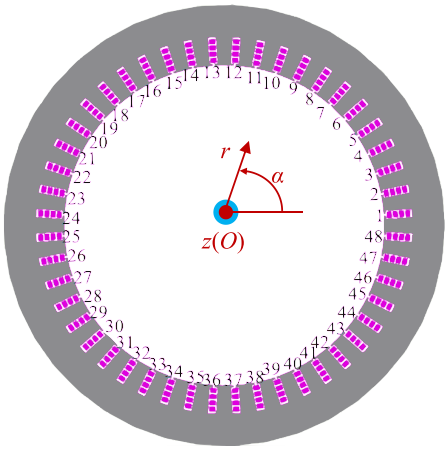

FIGURE 1. The cylindrical coordinate system O-$r\alpha z$ of IPMSM.

TABLE 2. The winding distribution of 4 layered flat wires of IPMSM.

Layer No. \ Slot No.	1	2	3	4	5	6	7	8	9	10	11	12
	13	14	15	16	17	18	19	20	21	22	23	24
	25	26	27	28	29	30	31	32	33	34	35	36
	37	38	39	40	41	42	43	44	45	46	47	48
1	-C	+B	+B	-A	-A	+C	+C	-B	-B	+A	+A	-C
2	-C	+B	+B	-A	-A	+C	+C	-B	-B	+A	+A	-C
3	+B	+B	-A	-A	+C	+C	-B	-B	+A	+A	-C	-C
4	+B	+B	-A	-A	+C	+C	-B	-B	+A	+A	-C	-C

$$B_{arl\_i}^{less}(r,\alpha,z,t) = I_{l\_i}(t) \sum_{q=1}^{\infty} B_{qr}(r) \cos[q(\alpha - \alpha_l)] \tag{4}$$

$$B_{atl\_i}^{less}(r,\alpha,z,t) = I_{l\_i}(t) \sum_{q=1}^{\infty} B_{qt}(r) \sin[q(\alpha - \alpha_l)] \tag{5}$$

where, I_{l_i} is the current in the l^{th} coil, i represents Phase A, Phase B, or Phase C, $I_{l\_i} \in \{I_A(t), I_B(t), I_C(t)\}$, q is the winding distribution order, B_{qr} and B_{qt} are the ampitudes of the q-order radial and tangential flux density when unit amplitude current is passed through the l^{th} coil, respectively, α_l is the angle of the center of the l^{th} coil.

Multiple coils or groups of coils constitute windings based on a certain distribution rule. The ARF of IPMSM can be equivalent to the superposition of magnetic fields of these multiple coils or groups of coils [26], [27]. Therefore, investigation of the winding distribution rule is the premise of analytical calculation of ARF of IPMSM. In this paper, because the greatest common divisor of the pole pair number and the slot number is equal to $N = \text{GCD}(p, Q_s) = 4$, the unit motors number is $N = 4$. Therefore, the winding distribution of the 4 layered flat wires repeats four times in the stator slots, shown in Table 2.

Based on the right hand rule, the coil magnetic field vector star chart of MFWW of IPMSM can be derived further, shown in Fig. 2. If upper and lower case letters represent forward and

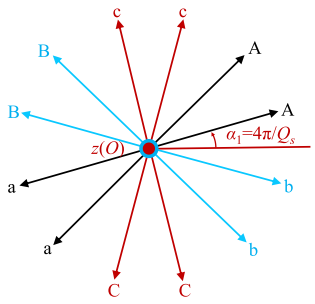

FIGURE 2. The coil magnetic field vector star chart of MFWW.

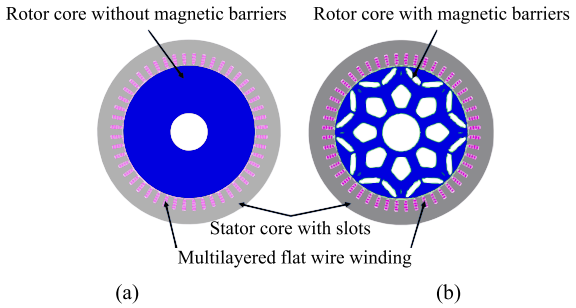

FIGURE 3. Two static magnetic field finite element models of air-gap permeance. (a) IPMSM without magnetic barriers. (b) IPMSM with magnetic barriers.

backward windings respectively, the magnetic field vector of each unit motor can be expressed as AAccBBaaCCbb.

Therefore, the ideal ARF of MFWW can be expressed as the superposition of ARFs of all the coils:

$$B_{ar}^{less}(r,\alpha,z,t) = \sum_{l=1}^{Q} B_{arl\_i}(r,\alpha,z,t) \tag{6}$$

$$B_{at}^{less}(r,\alpha,z,t) = \sum_{l=1}^{Q} B_{atl\_i}(r,\alpha,z,t) \tag{7}$$

where, Q is the coil number.

C. 3-D RELATIVE PERMEANCE FUNCTIONS

The stator slotting and the magnetic barriers of MSP rotor usually change the magnetic path reluctance and further affect the ARF.

In order to consider the stator slotting effects, an effective 2-D complex relative air-gap permeance function has been derived in [12]. In order to consider the influence of axial direction, it is expanded into 3-D complex relative permeance function in this paper:

$$\begin{aligned}\lambda_s(r,\alpha,z) &= \lambda_{sa}(r,\alpha,z) + j\cdot\lambda_{sb}(r,\alpha,z)\\ &= \left[\lambda_{sa0} + \sum_{\mu}^{N_\mu}\lambda_{sa\mu}cos(\mu Q_s\alpha)\right]\\ &\quad + j\cdot\left[\sum_{\mu}^{N_\mu}\lambda_{sb\mu}sin(\mu Q_s\alpha)\right]\end{aligned} \tag{8}$$

where, λ_{sa} and λ_{sb} are the real part and the imaginary part of the complex relative air-gap permeance function considering the stator slotting effects, respectively, j is the imaginary symbol, $\lambda_{sa\mu}$ and $\lambda_{sb\mu}$ are coefficients of Fourier series of the real part and the imaginary part, respectively, λ_{sa0} is constant of the real part, N_μ is the highest order of Fourier series.

In order to consider the permeance fluctuations caused by magnetic barriers of the rotor, numerical-analytical coupling methods, in which a fictitious magnet with a constant magnetomotive force is adopted to excite a slotless finite element model without magnetic barriers and a slotless finite element model with magnetic barriers, were developed in [8] and [28]. However, different fictitious magnet might lead to a different non-homogeneously saturated rotor [15]. In other words, the calculation methods of relative permeance function caused by magnetic barriers of the rotor in [8] and [28] depend on the parameter selection of the fictitious magnet. Therefore, a different method, in which a slotting finite element model without magnetic barriers and a slotting finite element model with magnetic barriers are excited by the ARF caused by MFWW at arbitrary time, is proposed to predict the relative permeance function caused by magnetic barriers of the rotor in this paper, shown in Fig. 3. The real part and the imaginary part of relative permeance caused by magnetic barriers of the rotor can be expressed [8], [28]:

$$\begin{aligned}&\lambda_{ra}^{*}(r,\alpha)\\ &= \frac{B_{ra\_r}(r,\alpha)B_{ra\_unr}(r,\alpha) + B_{ra\_t}(r,\alpha)B_{ra\_unt}(r,\alpha)}{B_{ra\_unr}^{2}(r,\alpha) + B_{ra\_unt}^{2}(r,\alpha)}\end{aligned} \tag{9}$$

$$\begin{aligned}&\lambda_{rb}^{*}(r,\alpha)\\ &= \frac{B_{ra\_r}(r,\alpha)B_{ra\_unt}(r,\alpha) - B_{ra\_t}(r,\alpha)B_{ra\_unr}(r,\alpha)}{B_{ra\_unr}^{2}(r,\alpha) + B_{ra\_unt}^{2}(r,\alpha)}\end{aligned} \tag{10}$$

where, B_{ra_unr} and B_{ra_unt} are the radial component and the tangential component of air-gap magnetic field without magnetic barrier, respectively, $B_{ra\_r}(r,\alpha)$ and $B_{ra\_t}(r,\alpha)$ are the radial component and the tangential component of air-gap magnetic field with magnetic barrier, respectively.

The rotor rotates at angular speed ω_r and passes through time t. Due to periodicity, (9) and (10) can be expressed as Fourier series [8], [28]:

$$\begin{aligned}\lambda_r^{*}(r,\alpha,t) &= \lambda_{ra}^{*}(r,\alpha,t) + j\cdot\lambda_{rb}^{*}(r,\alpha,t)\\ &= \left\{\lambda_{ra0} + \sum_{k}^{N_k}\lambda_{rak}\cos\left[2kp\left(\omega_r t+\alpha\right)\right]\right\}\\ &\quad + j\cdot\left\{\sum_{k}^{N_k}\lambda_{rbk}\sin\left[2kp\left(\omega_r t+\alpha\right)\right]\right\}\end{aligned} \tag{11}$$

where, λ_{rak} and λ_{rbk} are the real part and the imaginary part of the complex relative air-gap permeance function considering the magnetic barriers of the rotor, respectively, λ_{ra0} is constant of the real part, N_k is the highest order of Fourier series.

However, the 2-D analytical methods in [8] and [28] are not applicable to the relative permeance calculation caused by the magnetic barriers of MSP. As a consequence, a 3-D relative permeance of magnetic barriers of the rotor is presented in

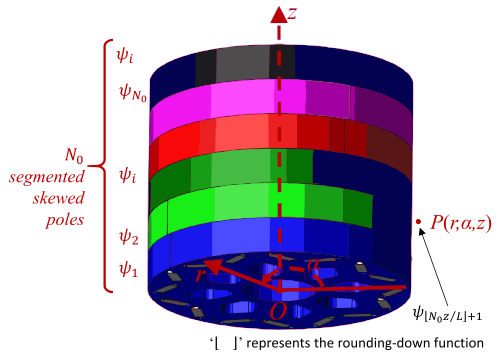

FIGURE 4. The skew angle of any point P in space for MSP.

this paper. The axial length of the rotor is L, and the rotor is evenly divided into N_0 segments. The skew angle corresponding to the i^{th} Segment is ψ_i, shown in Fig. 4. For any point $P(r, \alpha, z)$ in space, its skew angle should be $\psi_{\lfloor Nz/L \rfloor+1}$, where '$\lfloor\ \rfloor$' represents the rounding-down function. Therefore, the relative permeance of the magnetic barriers of the MSP rotor can be expressed:

$$\begin{aligned}&\lambda_r(r,\alpha,z,t)\\&=\lambda_{ra}(r,\alpha,z,t)+j\cdot\lambda_{rb}(r,\alpha,z,t)\\&=\left\{\lambda_{ra0}+\sum_k^{N_k}\lambda_{rak}\cos\left[2kp\left(\omega_r t+\alpha+\psi_{\lfloor Nz/L\rfloor+1}\right)\right]\right\}\\&\quad+j\cdot\left\{\sum_k^{N_k}\lambda_{rbk}\sin\left[2kp\left(\omega_r t+\alpha+\psi_{\lfloor Nz/L\rfloor+1}\right)\right]\right\}\end{aligned}\tag{12}$$

D. ARF OF IPMSM WITH MSP AND MFWW

The stator slotting and the magnetic barriers of the MSP rotor can change the relative permeance and affect the ARF of IPMSM with MSP and MFWW. Therefore, the radial and tangential components of ARF can be expressed [12]:

$$\begin{aligned}B_{ar}(r,\alpha,z,t)&=\left[B_{ar}^{less}\cdot\lambda_{ra}+B_{at}^{less}\cdot\lambda_{rb}\right]\cdot\lambda_{sa}\\&\quad+\left[B_{at}^{less}\cdot\lambda_{ra}-B_{ar}^{less}\cdot\lambda_{rb}\right]\cdot\lambda_{sb}\end{aligned}\tag{13}$$

$$\begin{aligned}B_{at}(r,\alpha,z,t)&=\left[B_{at}^{less}\cdot\lambda_{ra}-B_{ar}^{less}\cdot\lambda_{rb}\right]\cdot\lambda_{sa}\\&\quad-\left[B_{ar}^{less}\cdot\lambda_{ra}+B_{at}^{less}\cdot\lambda_{rb}\right]\cdot\lambda_{sb}\end{aligned}\tag{14}$$

By Substituting (1)-(8) and (12) into (13) and (14), a 3-D analytical model of ARF of IPMSM with MSP and MFWW considering current harmonics can be obtained:

$$\begin{aligned}&B_{ar}(r,\alpha,z,t)\\&=\left\{\left\{\sum_{l=1}^{Q}I_{l\_i}(t)\sum_{q=1}^{\infty}B_{qr}(r)\cos\left[q(\alpha-\alpha_l)\right]\right\}\right.\\&\quad\cdot\left\{\lambda_{ra0}+\sum_k^{N_k}\lambda_{rak}\cos\left[2kp\left(\omega_r t+\alpha+\psi_{\lfloor Nz/L\rfloor+1}\right)\right]\right\}\\&\quad+\left\{\sum_{l=1}^{Q}I_{l\_i}(t)\sum_{q=1}^{\infty}B_{qt}(r)\sin\left[q(\alpha-\alpha_l)\right]\right\}\\&\quad\left.\cdot\left\{\sum_k^{N_k}\lambda_{rbk}\sin\left[2kp\left(\omega_r t+\alpha+\psi_{\lfloor Nz/L\rfloor+1}\right)\right]\right\}\right\}\\&\quad\cdot\left[\lambda_{sa0}+\sum_\mu^{N_\mu}\lambda_{sa\mu}\cos\left(\mu Q_s\alpha\right)\right]\\&\quad+\left\{\left\{\sum_{l=1}^{Q}I_{l\_i}(t)\sum_{q=1}^{\infty}B_{qt}(r)\sin\left[q(\alpha-\alpha_l)\right]\right\}\right.\\&\quad\cdot\left\{\lambda_{ra0}+\sum_k^{N_k}\lambda_{rak}\cos\left[2kp\left(\omega_r t+\alpha+\psi_{\lfloor Nz/L\rfloor+1}\right)\right]\right\}\\&\quad\left.-\left\{\sum_{l=1}^{Q}I_{l\_i}(t)\sum_{q=1}^{\infty}B_{qr}(r)\cos\left[q(\alpha-\alpha_l)\right]\right\}\right.\\&\quad\left.\cdot\left\{\sum_k^{N_k}\lambda_{rbk}\sin\left[2kp\left(\omega_r t+\alpha+\psi_{\lfloor Nz/L\rfloor+1}\right)\right]\right\}\right\}\\&\quad\cdot\left[\sum_\mu^{N_\mu}\lambda_{sb\mu}\sin\left(\mu Q_s\alpha\right)\right]\end{aligned}\tag{15}$$

$$\begin{aligned}&B_{at}(r,\alpha,z,t)\\&=\left\{\left\{\sum_{l=1}^{Q}I_{l\_i}(t)\sum_{q=1}^{\infty}B_{qt}(r)\sin\left[q(\alpha-\alpha_l)\right]\right\}\right.\\&\quad\cdot\left\{\lambda_{ra0}+\sum_k^{N_k}\lambda_{rak}\cos\left[2kp\left(\omega_r t+\alpha+\psi_{\lfloor Nz/L\rfloor+1}\right)\right]\right\}\\&\quad-\left\{\sum_{l=1}^{Q}I_{l\_i}(t)\sum_{q=1}^{\infty}B_{qr}(r)\cos\left[q(\alpha-\alpha_l)\right]\right\}\\&\quad\left.\cdot\left\{\sum_k^{N_k}\lambda_{rbk}\sin\left[2kp\left(\omega_r t+\alpha+\psi_{\lfloor Nz/L\rfloor+1}\right)\right]\right\}\right\}\\&\quad\cdot\left[\lambda_{sa0}+\sum_\mu^{N_\mu}\lambda_{sa\mu}\cos\left(\mu Q_s\alpha\right)\right]\\&\quad-\left\{\left\{\sum_{l=1}^{Q}I_{l\_i}(t)\sum_{q=1}^{\infty}B_{qr}(r)\cos\left[q(\alpha-\alpha_l)\right]\right\}\right.\\&\quad\cdot\left\{\lambda_{ra0}+\sum_k^{N_k}\lambda_{rak}\cos\left[2kp\left(\omega_r t+\alpha+\psi_{\lfloor Nz/L\rfloor+1}\right)\right]\right\}\\&\quad+\left\{\sum_{l=1}^{Q}I_{l\_i}(t)\sum_{q=1}^{\infty}B_{qt}(r)\sin\left[q(\alpha-\alpha_l)\right]\right\}\\&\quad\left.\cdot\left\{\sum_k^{N_k}\lambda_{rbk}\sin\left[2kp\left(\omega_r t+\alpha+\psi_{\lfloor Nz/L\rfloor+1}\right)\right]\right\}\right\}\\&\quad\cdot\left[\sum_\mu^{N_\mu}\lambda_{sb\mu}\sin\left(\mu Q_s\alpha\right)\right]\end{aligned}\tag{16}$$

Based on (15) and (16), the spatial order and frequency features of ARF can be derived, in Table 3. The low-order current harmonics and the high-order sideband current harmonics do not change the spatial order q of the ideal ARF, but the frequency components hf_c and $a_nf_s \pm b_{n,k}f_c$ in ARF are added respectively. On the one hand, spatial orders 0 and μQ_s, and the frequency 0 Hz in relative permeance appear due to the stator slotting. On the other hand, the magnetic barriers of the rotor generate the relative permeance with the spatial orders 0 and $2kp$, and the frequencies 0 Hz and $2kf_c$ Hz. As a result, these factors significantly influence the spatial order and frequency features of ARF. Its main spatial orders are q, $q \pm \mu Q_s$, $q \pm 2kp$, and $q \pm 2kp \pm \mu Q_s$. Its prime frequencies are f_c, hf_c, $a_nf_s \pm b_{n,k}f_c$, $(2k \pm 1)f_c$, $(2k \pm h)f_c$, and $a_nf_s \pm (b_{n,k} + 2k)f_c$.

III. VALIDATION OF PROPOSED MODEL

A. COMPARISON BETWEEN ANALYTICAL AND FEM RESULTS OF ARF

In order to verify the proposed analytical model, the analytical results and the FEM results of ARF at the rated

TABLE 3. Spatial order and frequency of ARF.

Parameters	Spatial order\-	Frequency\Hz
$B_{ar}^{less}(r,\alpha,z,t)$ $B_{at}^{less}(r,\alpha,z,t)$	q	0
$\lambda_{sa}(r,\alpha,z)$	0	0
	μQ_s	0
$\lambda_{sb}(r,\alpha,z)$	μQ_s	0
$\lambda_{ra}(r,\alpha,z,t)$	0	$2kf_c$
	$2kp$	$2kf_c$
$\lambda_{rb}(r,\alpha,z,t)$	$2kp$	$f_c, hf_c, a_nf_s \pm b_{n,k}f_c$
$B_{ar}(r,\alpha,z,t)$ $B_{at}(r,\alpha,z,t)$	q	$f_c, hf_c, a_nf_s \pm b_{n,k}f_c$
	$q \pm \mu Q_s$	$(2k \pm 1)f_c, (2k \pm h)f_c,$ $a_nf_s \pm (b_{n,k} + 2k)f_c$
	$q \pm 2kp$	$(2k \pm 1)f_c, (2k \pm h)f_c,$ $a_nf_s \pm (b_{n,k} + 2k)f_c$
	$q \pm 2kp$ $\pm \mu Q_s$	0

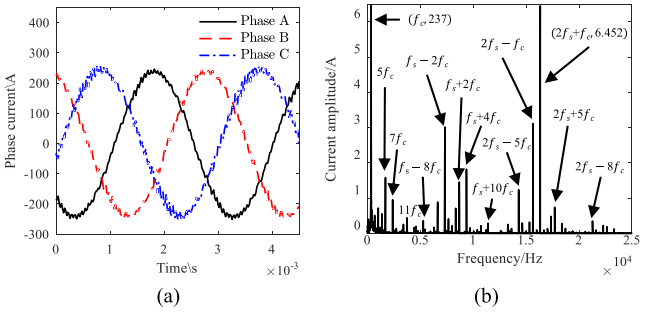

FIGURE 5. Phase currents collected by an experiment. (a) Time history. (b) Amplitude-frequency characteristics.

speed 5100 rpm and the load torque 100 N·m are compared in this chapter. Temperature of the FEM model is setted to 90 degrees Celsius.

Three phase currents were measured through experiment, shown in Fig. 5. A large number of harmonic components result in unsmooth time history waveforms of phase currents. component of phase currents, but there are plenty of low-order current harmonics with frequencies hf_c and high-order sideband current harmonics with frequencies $a_nf_s \pm b_{n,k}f_c$.

The experimental phase currents are inputted into the proposed analytical model and the finite element model and then the ARF can be obtained, shown in Fig. 6, Fig. 7, and Fig.8. It can be concluded that the analytical results agree well with the FEM results.

The time history and the amplitude-frequency characteristics of ARF are demonstrated in Fig. 6. The fundamental current with the frequency f_c generates the fundamental ARF with the same frequency. Meanwhile, the low-order current harmonics with the frequencies hf_c and the high-order sideband current harmonics with the frequencies $a_nf_s \pm b_{n,k}f_c$

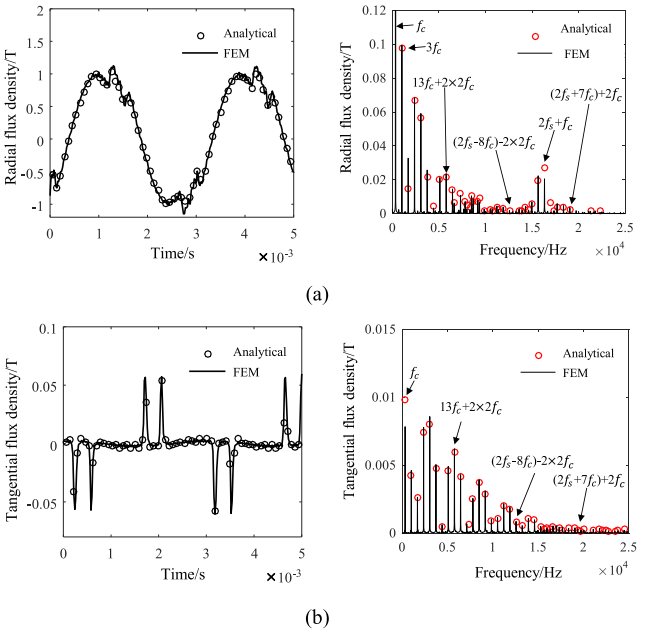

FIGURE 6. The time history and the amplitude-frequency characteristics of ARF. (a) Radial. (b) Tangential.

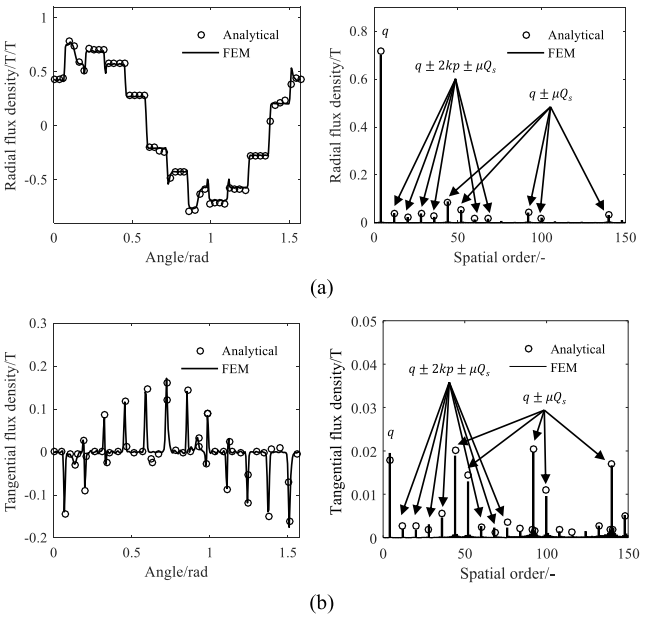

FIGURE 7. The spatial distribution and order characteristics of ARF. (a) Radial. (b) Tangential.

respectively generate the low-order and the high-order ARF harmonics with the same frequencies. Additionally, the magnetic barriers of the rotor cause new ARF harmonics. Under the action of the magnetic barriers and the current harmonics, ARF harmonics with new frequencies $(2k \pm 1)f_c$, $(2k \pm h)f_c$, $a_nf_s \pm (b_{n,k} + 2k)f_c$ occur.

The spatial distribution and order characteristics of ARF are displayed in Fig. 7. The spatial order of the ideal ARF is q. In addition, the stator slotting and the magnetic barriers of the rotor respectively generate new spatial orders μQ_s and $2kp$.

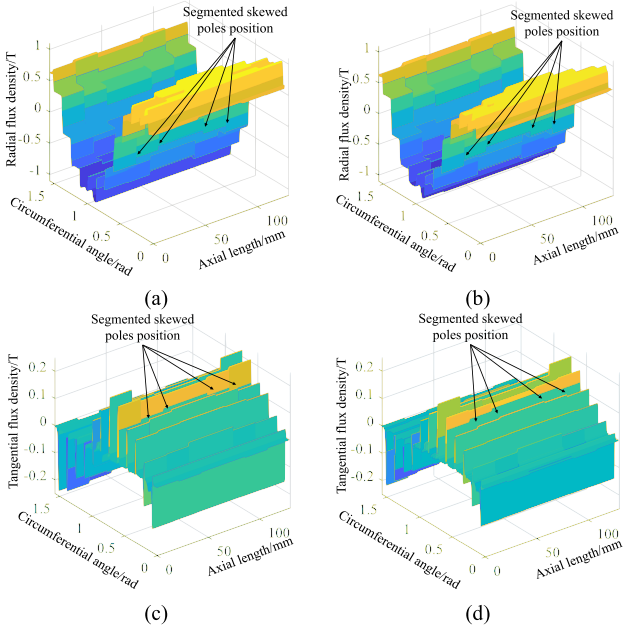

FIGURE 8. 3-D ARF of IPMSM with MSP and MFWW. (a) Radial (analytical). (b) Radial (FEM). (c) Tangential (analytical). (d) Tangential (FEM).

Therefore, the main spatial orders of the ARF of IPMSM are q, $q \pm \mu Q_s$, $q \pm 2kp$, and $q \pm 2kp \pm \mu Q_s$. The analytical results and the FEM results of the 3-D ARF of IPMSM with MSP and MFWW are exhibited in Fig. 8.

Although the MSP structure does not change the frequency characteristics and the spatial orders of ARF, it leads to the variation of the relative permeance along the axial direction because of the position modification of the magnetic barriers of the rotor and further causes the axial distribution variation of ARF.

The calculation efficiency of the analytical model and the FEM are compared further. In this case, a Dell Precision T5610 CTO Base with 16 cores, 96 G memory, and 3 TB hard disk is adopted in both calculation methods. The time and space sample points numbers of two methods are the same. They are 541 and 1001, respectively. The calculation time of the analytical model and the FEM are about 40 minutes and 40 hours, respectively. The former is only 1/60 of the latter. It can be concluded that the proposed analytical model in this paper is of high efficiency.

B. INDIRECT VALIDATION WITH ELECTROMAGNETIC TORQUE MEASUREMENT

Since ARF is difficult to be measured, measurement of the electromagnetic torque is adopted to indirectly verified the proposed model. Test bench for measurement is AVL Dyospirit 200/3.2-16 and the motor runs at the rated speed 5100 rpm and the load torque 100 N·m. The radial and tangential components of air gap magnetic field can be expressed by superposition method:

$$B_r(r,\alpha,z,t) = B_{ar}(r,\alpha,z,t) + B_{mr}(r,\alpha,z,t) \quad (17)$$

$$B_t(r,\alpha,z,t) = B_{at}(r,\alpha,z,t) + B_{mt}(r,\alpha,z,t) \quad (18)$$

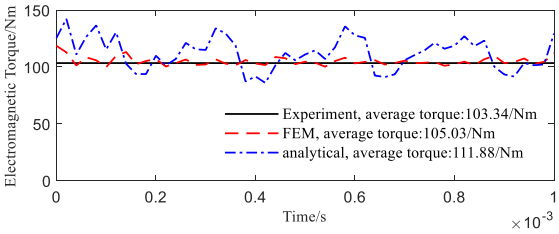

FIGURE 9. Electromagnetic torque comparison.

where, $B_{mr}(r,\alpha,z,t)$ and $B_{mt}(r,\alpha,z,t)$ are the radial and tangential components of OCAGF, respectively. They can be obtained by a 3-D Analytical Model of OCAGF of IPMSM [29].

By substituting (15) and (16) into (17) and (18), respectively, the air gap magnetic field is obtained and the electromagnetic torque can be expressed as [30]:

$$T_e = \frac{Lr^2}{\mu_0}\int_0^{2\pi}\left[B_r(\alpha,z,t)\cdot B_t(\alpha,z,t)\right]d\alpha \quad (19)$$

where, $B_r(\alpha,z,t)$ and $B_t(\alpha,z,t)$ are the radial and tangential components of air gap magnetic field in the middle of the airgap, respectively, r is the radius of the middle of airgap, μ_0 is the permeability in the airgap.

By substituting (17) and (18) into (19), electromagnetic torque is obtained. It is compared with experiment and FEM results, shown in Fig. 9. It can be concluded that the experiment results have less fluctuation than other results. FEM results are more approximate to the experiment results compared with analytical results. The differences between experiment results and two predicted results are 1.60% and 8.24%, which are not big in general. Experiment indirectly verifies the proposed model.

It needs to be explained that the experiment results fluctuates little due to the low sampling frequency of the sensor. In addition, because of the superposition method used in (17) and (18), part of the magnetic saturation in iron core is ignored, and then the resultant air gap magnetic field is overestimated. When this resultant air gap magnetic field is used in torque calculating, the calculated torque will be larger than experiment as it is shown in Fig. 9.

IV. CONCLUSION

In this paper, a 3-D analytical model of ARF of IPMSM with MSP and MFWW considering the low-order current harmonics and the high-order sideband current harmonics is proposed. The main conclusions are as follows:

1) The low-order current harmonics with frequencies hf_c and the high-order sideband current harmonics with frequencies $a_n f_s \pm b_{n,k} f_c$ generate the low-order and high-order ARF harmonics with the same frequencies, respectively. Additionally, the magnetic barriers of the rotor together with the current harmonics generate new ARF harmonics with frequencies $(2k \pm 1)f_c$, $(2k \pm h)f_c$, and $a_n f_s \pm (b_{n,k} + 2k)f_c$.

2) The stator slotting and the magnetic barriers of the rotor respectively bring in new spatial orders μQ_s and $2kp$ of ARF.

The main spatial orders of the ARF of IPMSM are q, $q \pm \mu Q_s$, $q \pm 2kp$, and $q \pm 2kp \pm \mu Q_s$.

3) Although the MSP structure does not change the frequency characteristics and the spatial orders of ARF, it leads to the variation of the relative permeance along the axial direction because of the position modification of the magnetic barriers of the rotor and further causes the axial distribution variation of ARF.

The proposed model combines two permeance functions considering stator slotting and rotor magnetic barriers and expands them from 2-D to 3-D. It can calculate ARF of IPMSM with different slot-pole combinations, rotor structures. However, its accuracy relies on precise calculation of 3-D relative permeance functions.

REFERENCES

[1] T. Noguchi, "Trends of permanent-magnet synchronous machine drives," *IEEJ Trans. Electr. Electron. Eng.*, vol. 2, pp. 125–142, Mar. 2007.

[2] Z. Azar, Z. Q. Zhu, and G. Ombach, "Investigation of torque–speed characteristics and cogging torque of fractional-slot IPM brushless AC machines having alternate slot openings," *IEEE Trans. Ind. Appl.*, vol. 48, no. 3, pp. 903–912, May/Jun. 2012.

[3] Q. Zhu, S. Ruangsinchaiwanich, N. Schofield, and D. Howe, "Reduction of cogging torque in interior-magnet brushless machines," *IEEE Trans. Magn.*, vol. 39, no. 5, pp. 3238–3240, Sep. 2003.

[4] M. Popescu, J. Goss, D. A. Staton, D. Hawkins, Y. C. Chong, and A. Boglietti, "Electrical Vehicles—Practical solutions for power traction motor systems," *IEEE Trans. Ind. Appl.*, vol. 54, no. 3, pp. 2751–2762, Jun. 2018.

[5] H.-J. Park and M.-S. Lim, "Design of high power density and high efficiency wound-field synchronous motor for electric vehicle traction," *IEEE Access*, vol. 7, pp. 46677–46685, 2019.

[6] S. Jurkovic, K. M. Rahman, J. C. Morgante, and P. J. Savagian, "Induction machine design and analysis for general motors e-Assist electrification technology," *IEEE Trans. Ind. Appl.*, vol. 51, no. 1, pp. 631–639, Jan. 2015.

[7] F. Lin, S. Zuo, W. Deng, and S. Wu, "Modeling and analysis of electromagnetic force, vibration, and noise in permanent-magnet synchronous motor considering current harmonics," *IEEE Trans. Ind. Electron.*, vol. 63, no. 12, pp. 7455–7466, Dec. 2016.

[8] F. Ma, H. Yin, L. Wei, L. Wu, and C. Gu, "Analytical calculation of armature reaction field of the interior permanent magnet motor," *Energies*, vol. 11, no. 9, p. 2375, Sep. 2018.

[9] K.-H. Shin, H.-W. Cho, S.-H. Lee, and J.-Y. Choi, "Armature reaction field and inductance calculations for a permanent magnet linear synchronous machine based on subdomain model," *IEEE Trans. Magn.*, vol. 53, no. 6, pp. 1–4, Jun. 2017.

[10] A. Rahideh and T. Korakianitis, "Analytical magnetic field distribution of slotless brushless permanent magnet motors—Part I. Armature reaction field, inductance and rotor eddy current loss calculations," *IET Electr. Power Appl.*, vol. 6, no. 9, pp. 628–638, Nov. 2012.

[11] M. Pourahmadi-Nakhli, A. Rahideh, and M. Mardaneh, "Analytical 2-D model of slotted brushless machines with cubic spoke-type permanent magnets," *IEEE Trans. Energy Convers.*, vol. 33, no. 1, pp. 373–382, Mar. 2018.

[12] D. Zarko, D. Ban, and T. A. Lipo, "Analytical calculation of magnetic field distribution in the slotted air gap of a surface permanent-magnet motor using complex relative air-gap permeance," *IEEE Trans. Magn.*, vol. 42, no. 7, pp. 1828–1837, Jul. 2006.

[13] X. Jin, O. Wasynczuk, and G. M. Shaver, "Computationally efficient and flexible magnetic-field-analysis-based scaling strategy for permanent-magnet machines," *IEEE Trans. Energy Convers.*, vol. 33, no. 3, pp. 1222–1232, Sep. 2018.

[14] D.-K. Lim, K.-P. Yi, D.-K. Woo, H.-K. Yeo, J.-S. Ro, C.-G. Lee, and H.-K. Jung, "Analysis and design of a multi-layered and multi-segmented interior permanent magnet motor by using an analytic method," *IEEE Trans. Magn.*, vol. 50, no. 6, pp. 1–8, Jun. 2014.

[15] M. Farshadnia, M. A. M. Cheema, R. Dutta, and J. E. Fletcher, "Analytical modeling of armature reaction air-gap flux density considering the non-homogeneously saturated rotor in a fractional-slot concentrated-wound IPM machine," *IEEE Trans. Magn.*, vol. 53, no. 2, pp. 1–12, Feb. 2017.

[16] G. Liu, L. Liu, Q. Chen, and W. Zhao, "Torque calculation of five-phase interior permanent magnet machine using improved analytical method," *IEEE Trans. Energy Convers.*, vol. 34, no. 2, pp. 1023–1032, Jun. 2019.

[17] Q. Li, T. Fan, X. Wen, and P. Ning, "An analytical approach to magnet eddy-current losses for interior permanent-magnet synchronous machines during flux weakening," *IEEE Trans. Magn.*, vol. 51, no. 8, pp. 1–9, Aug. 2015.

[18] M. S. Mirazimi and A. Kiyoumarsi, "Magnetic field analysis of multi-flux-barrier interior permanent-magnet motors through conformal mapping," *IEEE Trans. Magn.*, vol. 53, no. 12, pp. 1–12, Dec. 2017.

[19] K. Atallah, Z. Q. Zhu, and D. Howe, "Armature reaction field and winding inductances of slotless permanent-magnet brushless machines," *IEEE Trans. Magn.*, vol. 34, no. 5, pp. 3737–3744, Sep. 1998.

[20] Z. Tian, C. Zhang, and S. Zhang, "Analytical calculation of magnetic field distribution and stator iron losses for surface-mounted permanent magnet synchronous machines," *Energies*, vol. 10, no. 3, p. 320, Mar. 2017.

[21] C. Ma, Q. Li, H. Lu, Y. Liu, and H. Gao, "Analytical model for armature reaction of outer rotor brushless permanent magnet DC motor," *IET Electr. Power Appl.*, vol. 12, no. 5, pp. 651–657, May 2018.

[22] B. Gaussens, E. Hoang, O. de la Barriere, J. Saint-Michel, P. Manfe, M. Lecrivain, and M. Gabsi, "Analytical armature reaction field prediction in field-excited flux-switching machines using an exact relative permeance function," *IEEE Trans. Magn.*, vol. 49, no. 1, pp. 628–641, Jan. 2013.

[23] Z. Q. Zhu and D. Howe, "Instantaneous magnetic field distribution in brushless permanent magnet DC motors. III. effect of stator slotting," *IEEE Trans. Magn.*, vol. 29, no. 1, pp. 143–151, Jan. 1993.

[24] W. Liang, W. Fei, and P. C.-K. Luk, "An improved sideband current harmonic model of interior PMSM drive by considering magnetic saturation and cross-coupling effects," *IEEE Trans. Ind. Electron.*, vol. 63, no. 7, pp. 4097–4104, Jul. 2016.

[25] W. Deng and S. Zuo, "Comparative study of sideband electromagnetic force in internal and external rotor PMSMs with SVPWM technique," *IEEE Trans. Ind. Electron.*, vol. 66, no. 2, pp. 956–966, Feb. 2019.

[26] P. Liang, Y. Pei, F. Chai, Y. Bi, and S. Cheng, "An improved method for armature-reaction magnetic field calculation of interior permanent magnet motors," *IEEE Trans. Magn.*, vol. 52, no. 7, pp. 1–4, Jul. 2016.

[27] Q. Li, T. Fan, and X. Wen, "Armature-reaction magnetic field analysis for interior permanent magnet motor based on winding function theory," *IEEE Trans. Magn.*, vol. 49, no. 3, pp. 1193–1201, Mar. 2013.

[28] M. Fakam, M. Hecquet, V. Lanfranchi, and A. Randria, "Design and magnetic noise reduction of the surface permanent magnet synchronous machine using complex air-gap permeance," *IEEE Trans. Magn.*, vol. 51, no. 4, pp. 1–9, Apr. 2015.

[29] C. Ma, Y. An, H. Zhao, S. Guo, X. Yin, and H. Lu, "3-D analytical model and direct measurement method of ultra-thin open-circuit air-gap field of interior permanent magnet synchronous motor with multi-segmented skew poles and multi-layered flat wire windings for electric vehicles," *IEEE Trans. Energy Convers.*, early access, Mar. 23, 2020, doi: 10.1109/TEC.2020.2982450.

[30] S. M. Castano, B. Bilgin, J. Lin, and A. Emadi, "Radial forces and vibration analysis in an external-rotor switched reluctance machine," *IET Electr. Power Appl.*, vol. 11, no. 2, pp. 252–259, Feb. 2017.

CONGGAN MA (Member, IEEE) was born in Sichuan, China, in 1987. He received the B.S.E. and Ph.D. degrees in automotive engineering from Tongji University, Shanghai, China, in 2010 and 2014, respectively.

Since 2019, he has been a Professor with the College of Automotive Engineering, Harbin Institute of Technology at Weihai Campus, Weihai, China, where he was an Associate Professor from 2014 to 2019. His research interests include vehicle system dynamics and control, vehicle vibration and noise control, and vibration and noise of electrical machines.

Prof. Ma is a member of the IEEE Vehicular Technology Society, the Chinese Society of Theoretical and Applied Mechanics, and the Society of Automotive Engineering of China. He is a Senior Member of the Chinese Society for Vibration and Engineering.

JIAMING LI was born in Fujian, China, in 1993. He received the B.E. degree in automotive engineering from the Harbin Institute of Technology at Weihai Campus, Weihai, China, in 2015, where he is currently pursuing the M.S. degree with the School of Automotive Engineering.

His research interests include vehicle vibration, noise control, and fault diagnosis.

HUICHAO ZHAO (Member, IEEE) was born in Jilin, China, in 1975. He received the B.Sc. and M.Sc. degrees in automotive engineering from Jilin University, Changchun, China, in 1996 and 2005, respectively.

He is the Director of the Electric Drive System Institute, China First Automobile Works (FAW) Group, China. He is the main writer of the electric drive systems part of Made in China 2025. His research interests include the design and development of electric drive systems and the electromagnetic field analysis of electrical motors.

Mr. Zhao is a member of the China Electrotechnical Society and the IGBT Technology Innovation and Industry Alliance, China, and a Senior Advisor of Automotive Digest.

JINHAO WANG was born in Jilin, China, in 1986. He received the B.E. degree in mechanical engineering and automation and the M.E. degree in mechanical engineering from Tsinghua University, Beijing, China, in 2009 and 2012, respectively.

Since 2012, he has been an Engineer of the Electric Drive System Institute, China First Automobile Works (FAW) Group. His research interests include the thermal design of EV/HEV motors, heat management development, and multidiscipline coupled-field analysis for EV drive systems.

XIANGRUI YIN was born in Heilongjiang, China, in 1992. He received the B.Sc. and M.Sc. degrees in electrical engineering and automation from the Harbin Institute of Technology, Harbin, China, in 2014 and 2017, respectively.

Since 2017, he has been an Engineer with the Electric Drive System Institute, China First Automobile Works (FAW) Group, China. His research interests include the electromagnetic design of EV motors and the performance development of EV drive systems.

SHUGUANG ZUO, photograph and biography not available at the time of publication.

XUDONG WU, photograph and biography not available at the time of publication.

HAIFENG LU was born in Xinjiang, China, in 1994. He received the B.E. degree in energy and power engineering and the M.E. degree in automotive engineering from the Harbin Institute of Technology at Weihai Campus, Weihai, China, in 2017 and 2019, respectively.

His research interests include vehicle vibration and noise control, and the vibration and noise of electrical machines.